Growth and Electronic Properties of SnSe₂ Films on

Reconstructed, (111)-Oriented SrTiO₃ Substrates

Xi Dong, Tuan Anh Pham, Chunqiang Xu, Yining He, Wei Lai, Xianglin Ke, and Pengpeng

Zhang^{1,*}

¹Department of Physics and Astronomy, Michigan State University, East Lansing, MI 48824,

United States

²Department of Chemical Engineering and Materials Science, Michigan State University, East

Lansing, MI 48824, United States

Email: zhangpe@msu.edu

Keywords: charge density wave, metal dichalcogenides, 2D material, heterostructure, interfacial

charge transfer

ABSTRACT

Heterointerfaces and heterostructures offer unprecedented potential for tailoring physical

behaviors of two-dimensional materials. In this work, we investigate the growth and electronic

properties of SnSe₂ films on the 3x3 reconstructed (111)-oriented SrTiO₃ surface using scanning

tunneling microscopy/spectroscopy. A distinct coverage-dependent growth mode is identified,

which is unambiguously correlated to the spatial distribution of the electronic properties of SnSe₂

film. We further demonstrate that the interfacial modification using a van der Waals layered

1

material of low work function (1T'-WSe₂) between SnSe₂ films and the substrate effectively alters the growth and the electronic structures of SnSe₂. Our results provide useful insights into the interfacial phenomena that crucially influence the growth and functionalities of SnSe₂ films.

Introduction

Benefitting from the rapid advances in materials synthesis and processing, excellent control on the dimensionality of materials have been demonstrated.¹⁻² Remarkable physical phenomena emerge in zero-dimensional quantum dots,³ one-dimensional nanotubes,⁴ or two-dimensional monolayers.⁵ Furthermore, heterostructure construction between a low-dimensional material and a bulk substrate or another low-dimensional material may strengthen the existing properties of each constituent⁶ or even induce new physical behaviors,⁷ arising from the structural modification and electronic intertwining at the heterointerface, such as strain,⁸ charge transfer,⁹ Moiré pattern,¹⁰ electron-phonon coupling,¹¹ and proximity effect.⁷ For instance, FeSe monolayers grown on SrTiO₃ (STO) substrates revealed a drastic increase in its superconducting transition temperature (T_c) in comparison to the bulk counterpart, owing to the interfacial electron-phonon coupling and charge transfer.¹¹

More recently, charge density wave (CDW) and superconductivity (SC) were also induced in SnSe₂, an intrinsic layered semiconductor, via pressure,¹²⁻¹³ gating,¹⁴ formation of heterostructures¹⁵⁻¹⁶ or intercalations.¹⁷ Similar to high T_c superconductors,¹⁸ the electronic phase diagram of SnSe₂ exhibits a CDW phase adjacent to the SC phase,^{16, 19} which provides a potential platform for the study of correlated electronic behaviors near the two-dimensional (2D) limit. Furthermore, the formation of monolayer SnSe₂/1T'-WSe₂ core-shell heterostructures has been successfully demonstrated, bringing the 2D superconductor in adjacent to a 2D topological

insulator.²⁰ *Via* proximity effects, such lateral heterostructures offer promising routes to achieve topological superconductivity,^{7, 21} a key ingredient for the realization of Majorana fermions for fault tolerant quantum computing.²²

As pointed out in the previous studies, $^{14-17, 19, 23}$ CDW and SC transitions in the SnSe₂ heterostructure tie strongly to the amount of charge carriers near the Fermi level (FL) in SnSe₂, which is typically donated by the other constituent of the heterostructure. Thus, electron donating ability of the other constituent (usually the substrate) becomes very important. So far, the highest superconducting transition temperature ($T_c = \sim 8.3 \text{ K}$)¹⁶ in the SnSe₂ heterostructure was reported on the ultra-high vacuum (UHV) treated (001)-oriented STO substrates, since STO is an excellent electron donor hosting a two dimensional electron gas (2DEG) near the surface. ²⁴ Nonetheless, there have been discrepancies regarding the properties of SnSe₂ film grown on STO substrates. ¹⁵- ^{16, 19, 23} Detailed characterization of the growth morphology, the wetting layer, and its impacts on the characteristics of SnSe₂ thin film was largely missing in previous studies despite the critical influence of interface. Therefore, a systematic investigation of the SnSe₂/STO system on a microscopic scale is imperative for understanding the interfacial phenomena and a further approach to modify the interface to enhance the electron donating capability of the substrate will be invaluable.

In this work, we systematically investigate the growth morphologies and electronic structure variations in SnSe₂/(111)-oriented STO with and without interfacial modification using scanning tunneling microscopy/spectroscopy (STM/STS). (111)-oriented STO is selected as the substrate due to its symmetry matching to the lattice of SnSe₂. A distinct coverage-dependent growth of SnSe₂ is observed: in the direct contact regime, amorphous clusters are established to wet the substrate. Beyond the wetting layer, SnSe₂ forms a high-quality and continuous film that

conforms to the local height variations from the substrate and the wetting layer. Such conformation induces local strain and leads to variations in the film-substrate distance which is closely correlated to the electronic density of states near FL of the SnSe₂ film. These local nonuniformities profoundly impact the CDW behaviors of the SnSe₂ film, revealing the critical role of interfacial processes on the electronic properties of SnSe₂. To further illustrate the interfacial effects, 1T'-WSe₂ of low work function is utilized to modify the interface between the SnSe₂ film and the STO substrate, which leads to remarkably different growth and electronic structures in SnSe₂. Our study offers comprehensive understanding of the growth and local inhomogeneity of SnSe₂ films on STO substrates and provides valuable insights into the methodologies for further controlling the interfacial charge transfer, the key factor in determining the functionality of SnSe₂ films.

Methods

Sample preparation and characterization: The substrate preparation and sample growth were performed in a standard molecular beam epitaxy (MBE) chamber with base pressure <1×10° mBar. Before deposition, the Nb-doped (0.5% by weight) STO was cleaned using acetone and Isopropyl alcohol, then immediately transferred to the MBE chamber. The sample was treated at a rate of ~10°C/min with direct current and kept at 400 °C for 60mins to ensure proper degassing. The sample was then annealed at ~1150 °C for 60mins and cooled at the same rate (~10 °C/min) to create the proper surface reconstruction. SnSe₂ (1T'-WSe₂) was grown at a rate of ~0.2 (~1) monolayer/hour in the MBE chamber by co-deposition of pure Sn (W) and Se using an E-beam evaporator and a cracker cell, respectively. Excessive amount of Se was evaporated onto the substrate with chamber pressure reaching 1×10⁻⁸ mBar during the deposition. Substrate was maintained at ~185 °C during SnSe₂ growth and post annealed under Se flux to ~210 °C for 15 mins. 1T'-WSe₂ growth was carried out at a higher temperature of ~450 °C. The temperature of

the substrate was monitored by pyrometer at high temperatures (>600 °C) and by thermocouple mounted at the heating stage at lower temperatures. After the substrate treatment and film deposition, samples were transferred *in-situ* into an Omicron low temperature scanning tunneling microscope (STM) with base pressure < 2×10⁻¹¹ mBar for characterization. STM topography imaging was carried out at ~77.5 K except for those that reveal the CDW behaviors (at ~4.5 K). STS spectra were obtained at ~77.5 K using a lock-in amplifier with modulation signal set at 26 meV in amplitude and 1.3 kHz in frequency. The STM tip was calibrated by measuring reference spectra on silver substrate to avoid tip artifacts.

Results & Discussion

Distinct coverage-dependent growth of SnSe₂ on reconstructed STO(111)

Substrate surfaces play an indispensable role in the growth of high-quality thin films,^{1-2,25} which could also be responsible for tunning electronic properties of films.^{5-6, 9} Choosing a symmetry-matched supporting surface has profound benefits in heteroepitaxy.²⁶⁻²⁸ The (111)-oriented STO substrate is desirable since its symmetry matches to that of SnSe₂. While the surface of (111)-oriented STO is terminated either by Ti⁴⁺ and SrO₃⁴⁻, both of which are polar, its surface free energy can be reduced and the polarity be compensated by the electronic and structural reconstructions.²⁹⁻³⁴

As shown in Fig. 1a, after UHV annealing (see Methods), the substrate surface becomes primarily 3×3 reconstructed which can be modeled as a bilayer TiO_x termination with the absolute areal charge density equaling to half of that in the truncated bulk to compensate the surface polar instability.^{32,35} The height (Fig. 1b) across the step is measured to be ~ 0.23 nm, which agrees with the distance between the terraces of the same termination of (111)-oriented STO substrates.^{31-32,36} Local defects associated with adsorbates, Sr adatoms, and/or oxygen vacancies are observed (Fig.

S1 in the Supporting Information), which are common features of (111)-oriented STO surfaces.³³ Oxygen vacancies created during thermal annealing are expected to give rise to itinerant electrons that form a 2DEG near the surface.^{24, 37} The metallic transport behavior of both the Nb-doped (used for STM samples) and undoped (no bulk contribution to conductivity) substrates after identical thermal treatment are confirmed via four-probe measurements, as shown in Fig. S2. The UHV-annealed undoped sample reverses back to the insulating state after removal of the surface layers, supporting the formation of a 2DEG near surface after the thermal treatment. In addition, Fig. S3 shows that the conduction band minimum (CBM) of the STO substrate shifts toward the FL, which is associated with electron doping induced by Nb dopants and oxygen vacancies.

Upon deposition of SnSe₂ onto the 3 × 3 reconstructed, (111)-oriented STO surface, different growth modes are identified with increasing coverage (Fig. 1c-f). In the direct contact regime, the incoming atoms form small clusters that wet the underlying substrate surface (Fig. 1c and Fig. S4a-b). It should be noted that unlike other metal dichalcogenides (e.g. WSe₂, MoSe₂), SnSe₂ decomposes at temperatures above 240 °C which limits the growth temperature. Because of the relatively low deposition temperature, the diffusivity of adatoms on surface is limited.

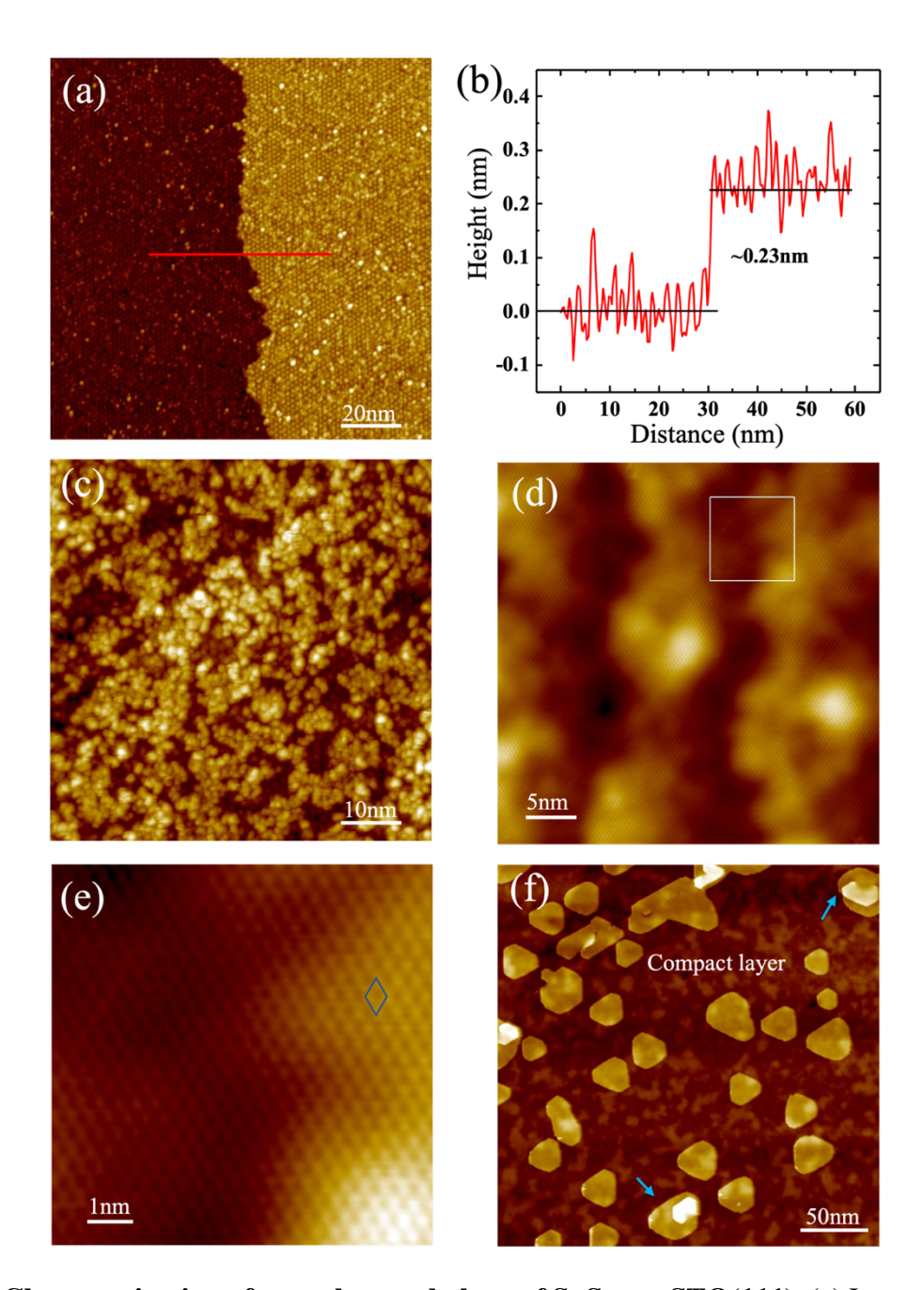


Figure 1. Characterization of growth morphology of SnSe₂ on STO(111). (a) Large scale STM image ($V_s = 2 \text{ V}$, $I_t = 5 \text{ pA}$) where the majority of the STO(111) surface forms 3×3 surface reconstruction. (b) Line profile across the red trace in (a), revealing the single step height of the STO(111) surface. (c) STM image ($V_s = 2.5 \text{ V}$, $I_t = 5 \text{ pA}$) showing the granular (e.g., cluster-like) growth of the SnSe₂ wetting layer that passivates the STO surface. (d) STM image ($V_s = 0.6 \text{ V}$, $I_t = 150 \text{ pA}$) illustrating the formation of continuous SnSe₂ compact layer beyond the wetting layer, which conforms to the substrate features such as steps of the STO(111) substrate. (e) Zoom-in STM image ($V_s = 0.6 \text{ V}$, $I_t = 150 \text{ pA}$) of the white box in (d), illustrating the lattice continuity across a substrate step with SnSe₂ unit cell labelled by blue rhombic. The film exhibits relatively low density of atomic defects. (f) STM image ($V_s = 2 \text{ V}$, $I_t = 5 \text{ pA}$) displaying the formation of

second layer islands on top of the compact SnSe₂ film. Blue arrows point to the islands that are evolving into spirals.

Further increase of the coverage beyond the wetting layer results in the formation of a compact SnSe₂ film (Fig. 1d-e). The film is conformal to the substrate features and has relatively low density of atomic defects. Figure 1e shows more details of the continuous SnSe₂ film across a substrate step, where the unit cell of SnSe₂ is marked by the blue rhombic. We speculate that the continuous and compact SnSe₂ layer is formed via the coalescing or coarsening of smaller islands (see discussion in Section II in the Supporting Information). During this process, some second layer islands that are partially connected to the underneath compact layer (Fig. 2a-b) are developed, likely facilitated by the unevenness of the substrate and the wetting layer. These partially connected second layer islands can be viewed as screw dislocations and act as seeds to drive the growth into a spiral form (Fig. 1f and Fig. S4c-d).^{25, 38} This thickness dependent growth of SnSe₂ is most pronounced on the STO substrate as compared to that on graphene¹⁵ or WSe₂²⁰, which could be attributed to the stronger interfacial interaction (see discussion in Section VI in the Supporting Information).

Evolution of SnSe₂ electronic structures across partially connected second layer islands

Now we will discuss the evolution of SnSe₂ electronic structures across a gradually climbing SnSe₂ island at the initial stage of the spiral formation (Fig. 2a-b). This study provides a unique opportunity to address the thickness-dependent interfacial charge transfer behaviors between SnSe₂ and STO substrate. To correctly interpretate the STS results, one should notice that the sensitivity of STS measurements to states of large parallel momentum critically depends on the tip-sample distance (see explanation in Section III of the Supporting Information).^{15, 39} There are three characteristic features expected on the SnSe₂ spectrum, i.e., valence band maximum

(VBM), CBM' and CBM.^{15, 40} The difference between the two conduction bands is that CBM' originates from Γ (k_{\parallel} = 0) point and CBM from M point of the Brillouin zone. At a large tip-sample distance (Fig. 2c), the bandgap between CBM' and VBM at the Γ point is measured, which decreases with increasing film thickness from the 1st to the 2nd SnSe₂ layer, likely originating from the reduced quantum confinement and the enhanced electrostatic screening.^{19,40} At the intermediate tip-sample distance (Fig. 2d), we start to observe some density of states (DOS) emerging below CBM' in both the first and the second layers. Upon bringing the tip-sample distance even closer (Fig. 2e), the tip sensitivity to states of large parallel momentum is increased and more detailed electronic structures are revealed, as evidenced by the observation of CBM at the M point (CBM(M)) in both the first and the second layers that are marked by the grey and purple triangles, respectively.

Tracing down from the second layer to the first layer along the partially connected region (Fig. 2b,e,f), the CBM(M) moves away from the FL, along the same trend as CBM'(Γ). Meanwhile, the tail-like DOS near the FL is increased. These tail-like DOS are referred to as "tail states" in the subsequent discussions. The tail states could stem from the 2DEG confinement or the virtually induced in-gap states at the interface, which are discussed in detail in Section III of the Supporting Information. These tail states were argued to be strongly correlated with the emerging CDW and SC phases in SnSe₂ thin films.^{15-16,19} Our experiment provides direct evidence that the DOS of these tail states sensitively depends on the film-to-substrate distance which continuously varies in the partially connected islands. As depicted in the STS line profile curves and the corresponding DOS heatmap (Fig. 2e-f), negligible DOS of the tail states is observed on the second layer (points 1-4), which gradually increases during the transition to the first layer (points 5-6) and becomes pronounced on the first layer (points 7-10). This observation strongly

supports the interfacial nature of the tail states and the associated emerging exotic phases in SnSe₂. As illustrated in Fig. 4 and Fig. S5, the CDW patterns are clearly resolved in the first SnSe₂ compact layer but largely absent in the second layer, thus correlating tightly to the DOS of the tail states near FL (Fig. 2e-f).

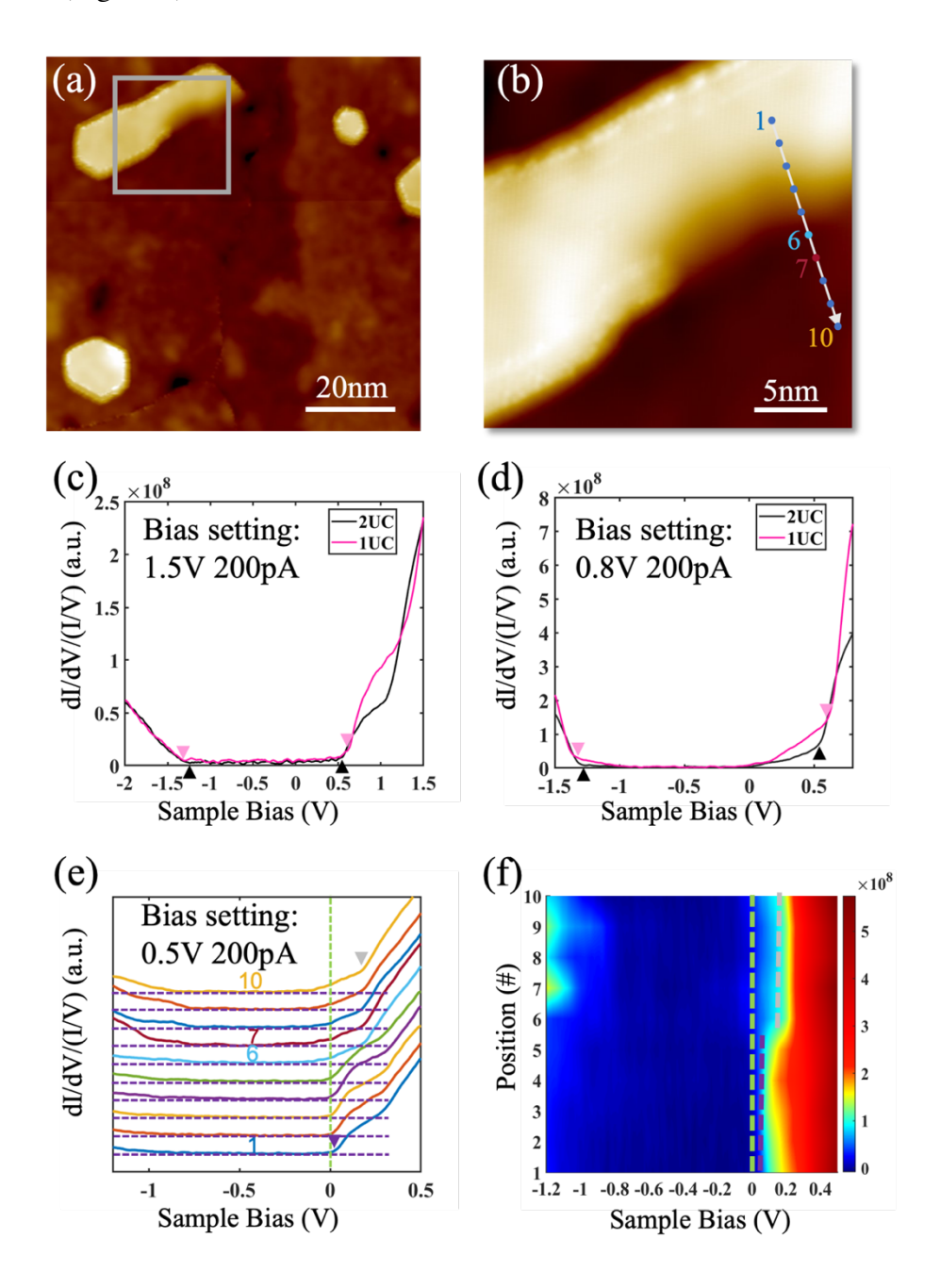


Figure 2. Charge transfer and electronic structure evolution across a "spiral"-grown $SnSe_2$ island. (a) Large scale STM image ($V_s = 2.5 \text{ V}$, $I_t = 5 \text{ pA}$) showing the coexistence of second layer

SnSe₂ islands that are either stand-alone or partially connected to the first layer. Zoom-in image of the grey box is shown in (b) ($V_s = 0.8 \text{ V}$, $I_t = 100 \text{ pA}$). (c-d) Normalized STS spectra taken on the monolayer (1UC, pink) and bilayer (2UC, black) SnSe₂ films at relatively large tip-sample distances. The pink and black triangles mark CBM' and VBM originating at the Γ point of the momentum space of 1UC and 2UC, respectively. (e) Normalized STS spectra taken along the white line in (b) from the second layer to the first layer at a reduced tip-sample distance, where CBM at the M point (larger parallel momentum) is identified, along with the emergence of a DOS tail penetrating through the Fermi level. The horizontal dashed lines provide eye guide for the ground of each spectrum. The grey and purple triangles mark the CBM position of the 1st and 2nd layer, respectively. (f) Corresponding DOS heatmap from STS spectra in (e) with x-axis, y-axis, and color contrast representing sample bias, point number, and intensity of DOS, respectively. Green dashed lines mark the Fermi level position in (e-f), and the grey and purple dashed lines in (f) mark the CBM position of the 1st and 2nd layer, respectively.

Correlation between interface morphology and electronic properties of SnSe₂ monolayer

As discussed above, Fig. 2 suggests that the property of the SnSe₂/STO system could be sensitively perturbed by the interface morphology as it varies the local distance between the film and the substrate. As shown in Fig. 1d-f, although the SnSe₂ compact layer displays relatively low density of atomic defects, there are height variations across the film. To further explore the impacts of these morphological features on the electronic properties of SnSe₂, we perform detailed analysis of the local strain, interfacial charge transfer, and CDW behaviors of the SnSe₂ compact layer. Figure 3a-b show the STM images of a continuous SnSe₂ film within the same STO terrace. The displayed dark and bright patches likely result from the conformation of the film over the nonuniform wetting layer/substrate, as indicated by the comparable height variations (Fig. 3d and inset of Fig. S4b). In Fig. 3d, the relatively flat area is furthest away from the STO substrate, thus appearing brightest in the corresponding STM image (Fig. 3a), while the pit area is closest to the substrate. Consistent with the earlier discussion, in-gap states are observed over the entire bandgap range on the pit area, and on the cone and the flat areas the density of these states decreases with the increasing distance to substrate (Fig. 3e). It is worth noting that the density of in-gap states near the VBM vary significantly and randomly, which is likely dominated by the localized defects

from the underlying wetting layer and the STO substrate such as oxygen vacancy (see discussion in Section III in the Supporting Information).⁴¹

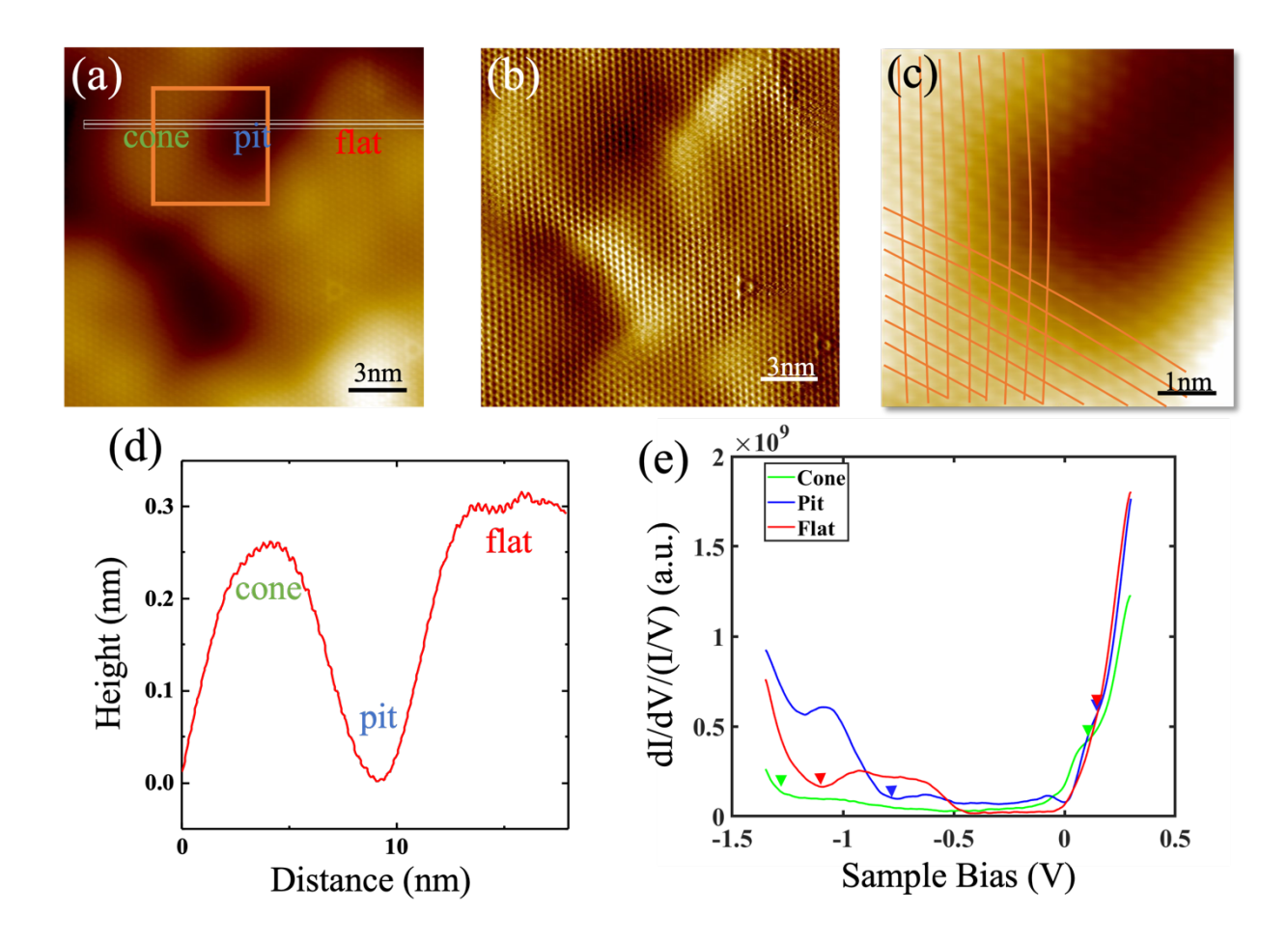


Figure 3. Strain variation in the as grown SnSe₂ film. (a) STM image ($V_s = 0.8 \text{ V}$, $I_t = 100 \text{ pA}$) of the SnSe₂ compact layer on top of a STO terrace, which reveals a pronounced height variation. The lattice continuity is clearly resolved in the current image ($V_s = 0.6 \text{ V}$, $I_t = 150 \text{ pA}$) in (b). (c) The local lattice distortions in the SnSe₂ film are illustrated in the zoom-in image (from the brown box in (a)), with the lines drawn to track the atom positions. (d) The height profile along the white trace in (a), where the cone, pit and flat regions are marked accordingly. (e) STS spectra (setpoint: $V_s = 0.3 \text{ V}$, $I_t = 200 \text{ pA}$) taken at the cone, pit, and flat regions, respectively. The arrows mark the onsets of CBM(M) and VBM(Γ).

Due to the height modulation, strain is also expected in SnSe₂. Figure 3c shows the lattice distortion tracked along the high symmetry directions of the SnSe₂ lattice, and table S1 lists the averaged local strain at the cone, the pit, and the relatively flat area, deduced from the Fast Fourier

Transformation (FFT) of the corresponding STM image shown in Fig. S6. Consistently, the flat area has nearly no strain, whereas the films at the cone and pit areas exhibit the tensile and compressive strain, respectively. SnSe₂ has positive Poisson ratio which is defined as $v = -\varepsilon_y/\varepsilon_x$ (x, y are commonly denoted as the zigzag and armchair direction, respectively).⁴² The fact that the strains are of the same sign along the x and y directions for both the pit and cone areas indicates a non-neglectable substrate interaction with the film. According to the previous DFT calculation,⁴³ biaxial tensile strain tends to increase the bandgap of SnSe₂ while compressive biaxial strain reduces the bandgap. Although the strain is not uniform in our sample, the general trend of the bandgap evolution discovered in our STS measurements (Fig. 3e) agrees well with the theory,⁴³ i.e., the bandgap of SnSe₂ is largest on the tensile-strained cone area and smallest on the compressive-strained pit area. On the flat area with very small compressive strain, the overall STS spectrum is comparable to the one shown in Fig. 2e, except the bump between -0.5V to -1.1V that likely arises from the localized defects on the substrate/wetting layer (see discussion in Section III in the Supporting Information).

Consequently, these electronic structure variations could result in perturbations to the physical behaviors of SnSe₂. As shown in the STM images taken at the different biases of the same area (Fig. 4a-b), local CDW patches, as illustrated by the dotted meshes that are commensurate to the 2 × 2 SnSe₂ lattice, are developed, but phase slips exist globally between these CDW domains. This is presumably due to the morphology and strain variations across the film. The line profile (Fig. 4c) taken along the blue mark shown in Fig. 4a clearly demonstrates the strain and height variations, where a pronounced CDW pattern is developed on the tensile-strained area (Fig. 4d). As discussed previously, the degree of interfacial charge transfer and the density of electrons in the SnSe₂ film play a dominant role in determining the phase diagram, such as the CDW transition

temperature in SnSe₂.¹⁹ Strain changes the bandgap of SnSe₂ film, whereas the density of tail states near FL, which is a strong indicator of the interfacial charge transfer, critically depends on the film thickness and film roughness. As CDW domains are developed heterogeneously across the SnSe₂ film, phase slips will emerge when these domains encounter with each other.

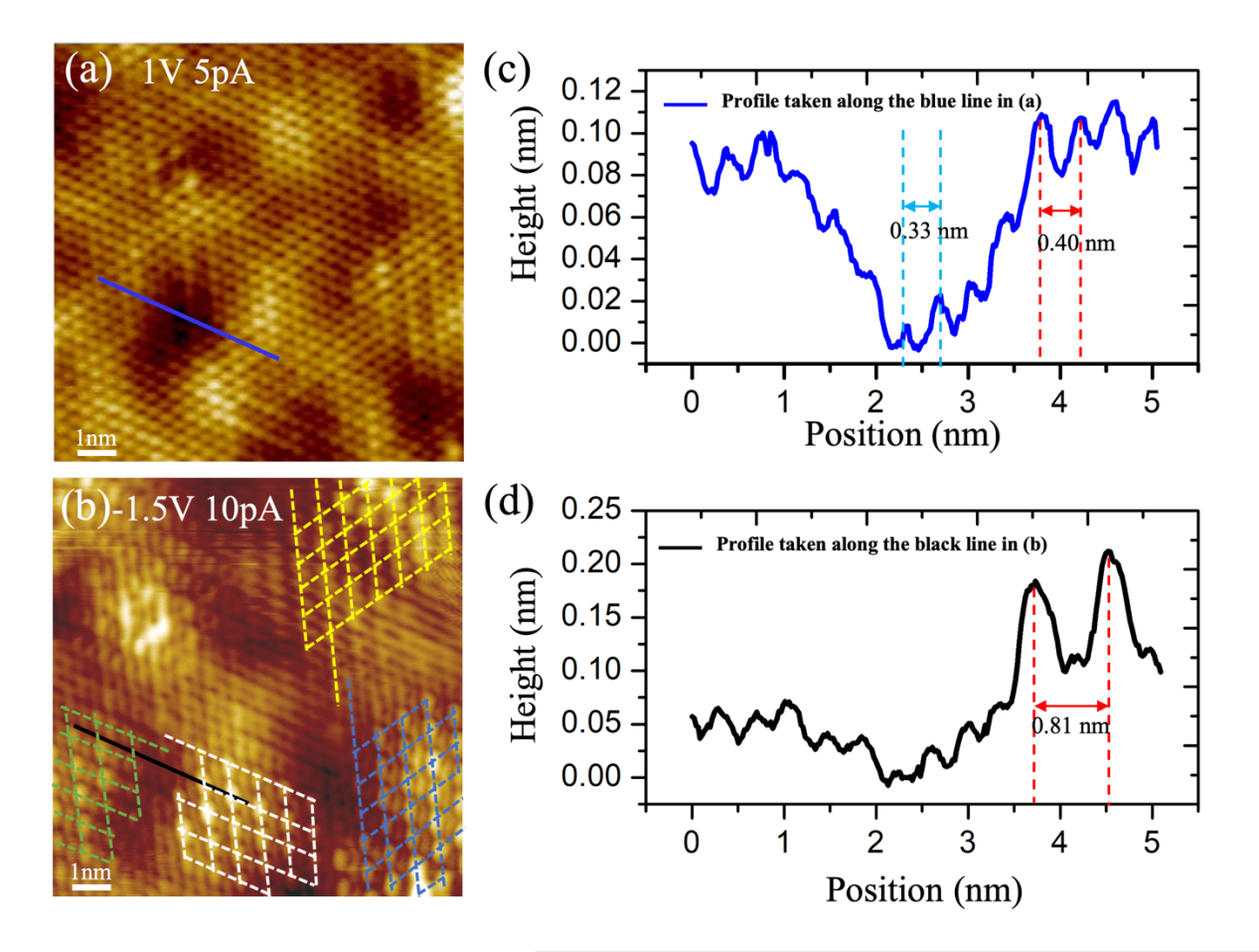


Figure 4. Charge density wave variations in the SnSe₂ compact layer on STO. (a) STM image $(V_s = 1.0 \text{ V}, I_t = 5 \text{ pA})$ of the SnSe₂ compact layer. (b) At a different bias $(V_s = -1.5 \text{ V}, I_t = 10 \text{ pA})$, the locally commensurate 2×2 CDW domains are observed, as outlined by the dotted meshes following the high symmetry directions of SnSe₂, that are separated by phase slips. The tip is functionalized to reveal the details of the CDW patterns. (c-d) Line-profile measurements across the blue and black marks in (a,b). Note that the two marks are at the same location. Dashed lines in (c) indicate the lattice constants in the pit and the cone areas, which are compressive and tensile strained, respectively. The 2×2 CDW periodicity on the cone area is indicated in (d).

Interfacial modification with WSe₂ monolayer

A natural question to ask is whether one can modify the interface to improve the growth of SnSe₂ on the STO substrate, and correspondingly the uniformity of its electronic properties. For this purpose, we explore the growth of another van der Waals layered material, WSe₂, prior to the deposition of SnSe₂. WSe₂ can be grown at much higher substrate temperatures (~450 °C to ~600 °C) without being decomposed, which should effectively reduce the formation of cluster layers on STO. Furthermore, WSe₂ has two different polymorphic phases, H and T', where the T'-WSe₂ has a work function of ~2.36 eV,⁴⁴ significantly lower than that of the STO substrate (~4.26 eV).⁴⁵ Covering the STO substrate with 1T'-WSe₂ will likely increase the ability of the substrate to transfer electrons to SnSe₂.

STM image of 1T'-WSe₂ depicts the characteristic stripe features (Fig. 5a and discussion in Section VI in the Supporting Information) with the periodic-like modulations along the stripes as observed in T'-WSe₂ grown on (100)-oriented STO(100). 46 Upon sequential deposition of SnSe₂ onto the (111)-oriented STO substrate that is partially covered with WSe₂, small SnSe₂ clusters are developed initially to fill the voids between WSe₂ islands, i.e., on the exposed STO surface (Fig. S7b), followed by the formation of a continuous and compact SnSe₂ film over the clusters and the WSe₂ islands (Fig. 5b). STS spectra taken on the SnSe₂/STO and SnSe₂/1T'-WSe₂/STO regions show distinct differences (Fig. 5c). The spectrum on SnSe₂/STO is consistent with that discussed in Fig. 2d, whereas the one on SnSe₂/1T'-WSe₂/STO behaves more metallic without an apparent band gap. Interfacial charge transfer is expected to be enhanced between SnSe₂ and 1T'-WSe₂/STO. In addition, orbital hybridization and electronic intertwining occur at the interface to drive the metallic-like STS features in SnSe₂ (see detailed discussion and calculations in Section VII in the Supporting Information). This result suggests that interfacial modification can effectively tailor the growth and electronic structures of SnSe₂ films. Since the exotic properties

like CDW and superconductivity in SnSe₂ stem from the interfacial phenomena, such modifications will open new routes for engineering the functionalities of SnSe₂. Furthermore, as suggested in Fig. S10, CDW is absent on SnSe₂/1T'-WSe₂/STO, in contrast to the scenario without the interfacial buffer layer, which could be related to the metallic-like electronic structures of SnSe₂/1T'-WSe₂/STO. Since the CDW phase is adjacent to the SC phase on the phase diagram of SnSe₂, SnSe₂/STO and SnSe₂/1T'-WSe₂/STO provide a valuable platform for investigating the correlation between CDW and superconductivity at low temperatures that is beyond the scope of this work.

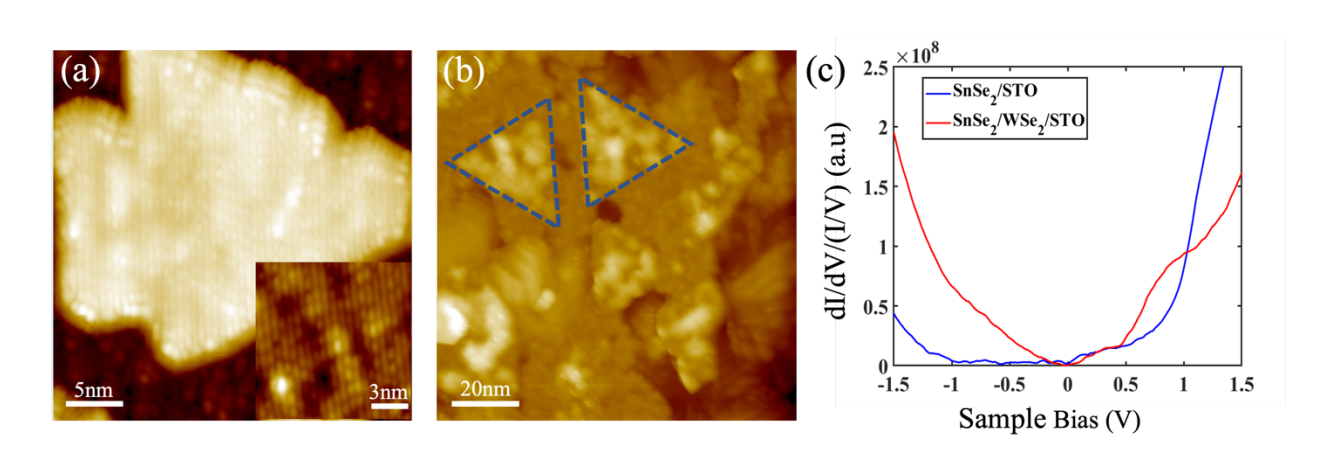


Figure 5. Electronic structures of SnSe₂/STO vs. SnSe₂/1T'-WSe₂/STO. (a) STM images ($V_s = 1 \text{ V}$, $I_t = 20 \text{ pA}$) of 1T'-WSe₂/STO showing characteristic stripe-like feature. Inset is the zoom-in image of the stripe structure. (b) STM image ($V_s = 2 \text{ V}$, $I_t = 5 \text{ pA}$) taken after the growth of a monolayer SnSe₂ on the STO with partially covered 1T'-WSe₂. The dashed blue triangles in (b) highlight the 1T'-WSe₂ islands underneath the monolayer SnSe₂. (c) STS spectra (setpoint: $V_s = 1.3 \text{ V}$, $I_t = 150 \text{ pA}$) taken on the SnSe₂/STO and SnSe₂/1T'-WSe₂/STO regions with the latter behaving more metallic.

Conclusion

For the SnSe₂ films grown on the reconstructed, (111)-oriented STO, we discover a coverage dependent growth mode and the formation of a "wetting" layer in the direct contact

regime. Although the subsequent SnSe₂ growth above the wetting layer empowers continuous and compact films conformal to the substrate with relatively low density of atomic defects, the height variation imparted from the wetting layer introduces strain and changes the distance between the SnSe₂ film and the STO substrate. We show that the low-energy physical behaviors of the SnSe₂/STO system strongly correlates to the interface morphology, the slight variations of which induces appreciable changes in the electronic structure, the degree of interfacial charge transfer, and hence the properties of SnSe₂. This provides a new perspective for understanding the controversial features of SnSe₂/STO reported in the earlier studies. ^{16,19,23} Furthermore, our results suggest that 1T'-WSe₂ of low work function might provide suitable interfacial modification to effectively reduce the formation of the wetting layer and to alter the electronic structures of SnSe₂ to be more metallic. Future studies on thus-grown films are warranted to explore the correlation between CDW and superconductivity in SnSe₂.

ASSOCIATED CONTENT

Supporting Information

See the supporting information for 2DEG and scanning tunneling spectroscopy on reconstructed STO surface, Characterization of the wetting layer growth and the formation of spirals in SnSe₂ film, Origin of the tail states and their relevance to the physical properties, Charge density wave variations in SnSe₂/STO, Local strain variations in SnSe₂ grown on STO, Growth morphology of SnSe₂ on WSe₂ covered STO, Interfacial interaction and electronic properties of SnSe₂ on WSe₂.

AUTHOR INFORMATION

Corresponding Author

* Pengpeng Zhang, Department of Physics and Astronomy, Michigan State University, East Lansing, MI 48824, United States. Email: zhangpe@msu.edu

Author Contributions

X. Dong, T. Pham, and P. P. Zhang designed the experiments and wrote the manuscript. X. Dong and T. Pham performed sample preparation and characterization. C. Xu and X. Ke performed the four-probe resistance measurement. Y. H and W. Lai conducted DFT calculations. P. P. Zhang supervised the project.

Notes

The authors have no conflicts to declare.

ACKNOWLEDGEMENTS

P. P. Zhang acknowledges the National Science Foundation (DMR-2112691). X. Dong and T. Pham thank the financial support from the U.S. Department of Energy (DOE), Office of Basic Energy Sciences, Division of Materials Sciences and Engineering under Award Number DE-SC0019120. X. Ke acknowledges the financial support by the National Science Foundation (DMR-2219046).

REFERENCES

- 1. Lasek, K.; Li, J. F.; Kolekar, S.; Coelho, P. M.; Guo, L. A.; Zhang, M.; Wang, Z. M.; Batzill, M., Synthesis and Characterization of 2D Transition Metal Dichalcogenides: Recent Progress from a Vacuum Surface Science Perspective. *Surf Sci Rep* **2021**, *76*, 100523.
- 2. Zhang, Y.; Yao, Y.; Sendeku, M. G.; Yin, L.; Zhan, X.; Wang, F.; Wang, Z.; He, J., Recent Progress in CVD Growth of 2D Transition Metal Dichalcogenides and Related Heterostructures. *Adv Mater* **2019**, *31*, e1901694.
- 3. Bera, D.; Qian, L.; Tseng, T.-K.; Holloway, P. H., Quantum Dots and Their Multimodal Applications: A Review. *Mater* **2010**, *3*, 2260-2345.
- 4. Cambre, S.; Liu, M.; Levshov, D.; Otsuka, K.; Maruyama, S.; Xiang, R., Nanotube-Based 1D Heterostructures Coupled by van der Waals Forces. *Small* **2021**, *17*, e2102585.
- 5. Choi, W.; Choudhary, N.; Han, G. H.; Park, J.; Akinwande, D.; Lee, Y. H., Recent Development of Two-Dimensional Transition Metal Dichalcogenides and Their Applications. *Mater Today* **2017**, *20*, 116-130.
- 6. Seyler, K. L.; Zhong, D.; Huang, B.; Linpeng, X.; Wilson, N. P.; Taniguchi, T.; Watanabe, K.; Yao, W.; Xiao, D.; McGuire, M. A., et al., Valley Manipulation by Optically Tuning the Magnetic Proximity Effect in WSe₂/CrI₃ Heterostructures. *Nano Lett* **2018**, *18*, 3823-3828.
- 7. Wang, J.; Zhang, S. C., Topological States of Condensed Matter. *Nat Mater* **2017**, *16*, 1062-1067.
- 8. Peng, Z.; Chen, X.; Fan, Y.; Srolovitz, D. J.; Lei, D., Strain Engineering of 2D Semiconductors and Graphene: from Strain Fields to Band-Structure Tuning and Photonic Applications. *Light Sci Appl* **2020**, *9*, 190.
- 9. Li, W.; Qian, X.; Li, J., Phase Transitions in 2D Materials. *Nat Rev Mater* **2021**, *6*, 829-846.
- 10. Zhang, C.; Chuu, C. P.; Ren, X.; Li, M. Y.; Li, L. J.; Jin, C.; Chou, M. Y.; Shih, C. K., Interlayer Couplings, Moire Patterns, and 2D Electronic Superlattices in MoS₂/WSe₂ Hetero-Bilayers. *Sci Adv* **2017**, *3*, e1601459.
- 11. Zhang, H.; Zhang, D.; Lu, X.; Liu, C.; Zhou, G.; Ma, X.; Wang, L.; Jiang, P.; Xue, Q. K.; Bao, X., Origin of Charge Transfer and Enhanced Electron-Phonon Coupling in Single Unit-Cell FeSe Films on SrTiO₃. *Nat Commun* **2017**, *8*, 214.
- 12. Zhou, Y.; Zhang, B.; Chen, X.; Gu, C.; An, C.; Zhou, Y.; Cai, K.; Yuan, Y.; Chen, C.; Wu, H., et al., Pressure-Induced Metallization and Robust Superconductivity in Pristine 1T-SnSe₂. *Adv Electron Mater* **2018**, *4*, 1800155.
- 13. Ying, J.; Paudyal, H.; Heil, C.; Chen, X. J.; Struzhkin, V. V.; Margine, E. R., Unusual Pressure-Induced Periodic Lattice Distortion in SnSe₂. *Phys Rev Lett* **2018**, *121*, 027003.
- 14. Zeng, J.; Liu, E.; Fu, Y.; Chen, Z.; Pan, C.; Wang, C.; Wang, M.; Wang, Y.; Xu, K.; Cai, S., et al., Gate-Induced Interfacial Superconductivity in 1T-SnSe₂. *Nano Lett* **2018**, *18*, 1410-1415.
- 15. Zhang, Y. M.; Fan, J. Q.; Wang, W. L.; Zhang, D.; Wang, L. L.; Li, W.; He, K.; Song, C. L.; Ma, X. C.; Xue, Q. K., Observation of Interface Superconductivity in a SnSe2/Epitaxial Graphene van der Waals Heterostructure. *Phys Rev B* **2018**, *98*, 220508(R).
- 16. Shao, Z. B.; Fu, Z. G.; Li, S. J.; Cao, Y.; Bian, Q.; Sun, H. G.; Zhang, Z. Y.; Gedeon, H.; Zhang, X.; Liu, L. J., et al., Strongly Compressed Few-Layered SnSe₂ Films Grown on a SrTiO₃

- Substrate: The Coexistence of Charge Ordering and Enhanced Interfacial Superconductivity. *Nano Lett* **2019**, *19*, 5304-5312.
- 17. Song, Y. P.; Liang, X. W.; Guo, J. G.; Deng, J.; Gao, G. Y.; Chen, X. L., Superconductivity in Li-Intercalated 1T-SnSe₂ Driven by Electric Field Gating. *Phys Rev Mater* **2019**, *3*, 054804
- 18. Zhou, X.; Lee, W.-S.; Imada, M.; Trivedi, N.; Phillips, P.; Kee, H.-Y.; Törmä, P.; Eremets, M., High-Temperature Superconductivity. *Nat Rev Phys* **2021**, *3*, 462-465.
- 19. Wang, S. Z.; Zhang, Y. M.; Fan, J. Q.; Ren, M. Q.; Song, C. L.; Ma, X. C.; Xue, Q. K., Charge Density Waves and Fermi Level Pinning in Monolayer and Bilayer SnSe₂. *Phys Rev B* **2020**, *102*, 241408(R).
- 20. Dong, X.; Lai, W.; Zhang, P., Semiconductor to Topological Insulator Transition Induced by Stress Propagation in Metal Dichalcogenide Core—Shell Lateral Heterostructures. *Mater Horiz* **2021**, *8*, 1029-1036.
- 21. Fu, L.; Kane, C. L., Josephson Current and Noise at a Superconductor/Quantum-Spin-Hall-Insulator/Superconductor Junction. *Phys Rev B* **2009**, *79*, 161408(R).
- 22. Das Sarma, S.; Freedman, M.; Nayak, C., Majorana Zero Modes and Topological Quantum Computation. *Npj Quantum Inf* **2015**, *1*, 15001.
- 23. Mao, Y. H.; Ma, X. C.; Wu, D. X.; Lin, C.; Shan, H.; Wu, X. J.; Zhao, J.; Zhao, A. D.; Wang, B., Interfacial Polarons in van der Waals Heterojunction of Monolayer SnSe₂ on SrTiO₃ (001). *Nano Lett* **2020**, *20*, 8067-8073.
- 24. Walker, S. M.; de la Torre, A.; Bruno, F. Y.; Tamai, A.; Kim, T. K.; Hoesch, M.; Shi, M.; Bahramy, M. S.; King, P. D.; Baumberger, F., Control of a Two-Dimensional Electron Gas on SrTiO₃(111) by Atomic Oxygen. *Phys Rev Lett* **2014**, *113*, 177601.
- 25. Dong, X.; Yan, C.; Tomer, D.; Li, C. H.; Li, L., Spiral Growth of Few-Layer MoS₂ by Chemical Vapor Deposition. *Appl Phys Lett* **2016**, *109*, 051604.
- 26. Wakasugi, T.; Hirose, Y.; Nakao, S.; Sugisawa, Y.; Sekiba, D.; Hasegawa, T., High-Quality Heteroepitaxial Growth of Thin Films of the Perovskite Oxynitride CaTaO₂N: Importance of Interfacial Symmetry Matching between Films and Substrates. *ACS Omega* **2020**, *5*, 13396-13402.
- 27. Proffit, D. L.; Jang, H. W.; Lee, S.; Nelson, C. T.; Pan, X. Q.; Rzchowski, M. S.; Eom, C. B., Influence of Symmetry Mismatch on Heteroepitaxial Growth of Perovskite Thin Films. *Appl Phys Lett* **2008**, *93*, 111912.
- 28. Chen, P. Y.; Xu, W. S.; Gao, Y. K.; Warner, J. H.; Castell, M. R., Epitaxial Growth of Monolayer MoS₂ on SrTiO₃ Single Crystal Substrates for Applications in Nanoelectronics. *Acs Appl Nano Mater* **2018**, *1*, 6976-6988.
- 29. Noguera, C., Polar Oxide Surfaces. J Phys Condens Mat 2000, 12, R367-R410.
- 30. Russell, B. C.; Castell, M. R., $(13\times13)R13.9^{\circ}$ and $(7\times7)R19.1^{\circ}$ Reconstructions of the Polar SrTiO₃(111) Surface. *Phys Rev B* **2007**, *75*, 155433.
- 31. Russell, B. C.; Castell, M. R., Surface of Sputtered and Annealed Polar $SrTiO_3(111)$: TiO_x -Rich (n × n) Reconstructions. *J Phys Chem C* **2008**, *112*, 6538-6545.
- 32. Marks, L. D.; Chiaramonti, A. N.; Rahman, S. U.; Castell, M. R., Transition from Order to Configurational Disorder for Surface Reconstructions on SrTiO₃(111). *Phys Rev Lett* **2015**, *114*, 226101.
- 33. Feng, J.; Zhu, X.; Guo, J., Reconstructions on SrTiO₃(111) Surface Tuned by Ti/Sr Deposition. *Surf Sci* **2013**, *614*, 38-45.

- 34. Torrelles, X.; Cantele, G.; De Luca, G. M.; Di Capua, R.; Drnec, J.; Felici, R.; Ninno, D.; Herranz, G.; Salluzzo, M., Electronic and Structural Reconstructions of the Polar (111) SrTiO₃ Surface. *Phys Rev B* **2019**, *99*, 205421.
- 35. Liang, Y.; Wang, Y. D.; Liu, L. X.; Guo, Q. L.; Wang, W. H.; Yang, H.; Guo, J. D., Chemical Intermixing at Oxide Heterointerfaces with Polar Discontinuity. *Appl Phys Lett* **2018**, *112*, 231601.
- 36. Biswas, A.; Rossen, P. B.; Yang, C. H.; Siemons, W.; Jung, M. H.; Yang, I. K.; Ramesh, R.; Jeong, Y. H., Universal Ti-rich Termination of Atomically Flat SrTiO₃ (001), (110), and (111) Surfaces. *Appl Phys Lett* **2011**, *98*, 051904.
- 37. Walker, S. M.; Bruno, F. Y.; Wang, Z.; de la Torre, A.; Ricco, S.; Tamai, A.; Kim, T. K.; Hoesch, M.; Shi, M.; Bahramy, M. S., et al., Carrier-Density Control of the SrTiO₃ (001) Surface 2D Electron Gas studied by ARPES. *Adv Mater* **2015**, *27*, 3894-9.
- 38. Wu, J.; Hu, Z.; Jin, Z.; Lei, S.; Guo, H.; Chatterjee, K.; Zhang, J.; Yang, Y.; Li, B.; Liu, Y., et al., Spiral Growth of SnSe₂ Crystals by Chemical Vapor Deposition. *Adv Mater Interfaces* **2016**, *3*, 1600383.
- 39. Zhang, C.; Chen, Y.; Johnson, A.; Li, M. Y.; Li, L. J.; Mende, P. C.; Feenstra, R. M.; Shih, C. K., Probing Critical Point Energies of Transition Metal Dichalcogenides: Surprising Indirect Gap of Single Layer WSe₂. *Nano Lett* **2015**, *15*, 6494-500.
- 40. Gonzalez, J. M.; Oleynik, I. I., Layer-Dependent Properties of SnS₂ and SnSe₂ Two-Dimensional Materials. *Phys Rev B* **2016**, *94*, 125443.
- 41. Sitaputra, W.; Sivadas, N.; Skowronski, M.; Xiao, D.; Feenstra, R. M., Oxygen Vacancies on SrO-Terminated SrTiO₃(001) Surfaces Studied by Scanning Tunneling Spectroscopy. *Phys Rev B* **2015**, *91*, 205408.
- 42. Javed, Y.; Mirza, S. M.; Rafiq, M. A., Effect of Pressure on Mechanical and Thermal Properties of SnSe₂. *Int J Thermophys* **2021**, *42*, 146.
- 43. Huang, Y.; Ling, C.; Liu, H.; Wang, S.; Geng, B., Versatile Electronic and Magnetic Properties of SnSe₂ Nanostructures Induced by the Strain. *J Phys Chem C* **2014**, *118*, 9251-9260.
- 44. Lei, B.; Pan, Y.; Hu, Z.; Zhang, J.; Xiang, D.; Zheng, Y.; Guo, R.; Han, C.; Wang, L.; Lu, J., et al., Direct Observation of Semiconductor–Metal Phase Transition in Bilayer Tungsten Diselenide Induced by Potassium Surface Functionalization. *ACS Nano* **2018**, *12*, 2070-2077.
- 45. Zagonel, L. F.; Baurer, M.; Bailly, A.; Renault, O.; Hoffmann, M.; Shih, S. J.; Cockayne, D.; Barrett, N., Orientation-Dependent Work Function of In Situ Annealed Strontium Titanate. *J Phys-Condens Mat* **2009**, *21*, 314013.
- 46. Chen, W.; Hu, M.; Zong, J.; Xie, X.; Meng, Q.; Yu, F.; Wang, L.; Ren, W.; Chen, A.; Liu, G., et al., Epitaxial Growth of Single-Phase 1T'-WSe₂ Monolayer with Assistance of Enhanced Interface Interaction. *Adv Mater* **2021**, *33*, e2004930.

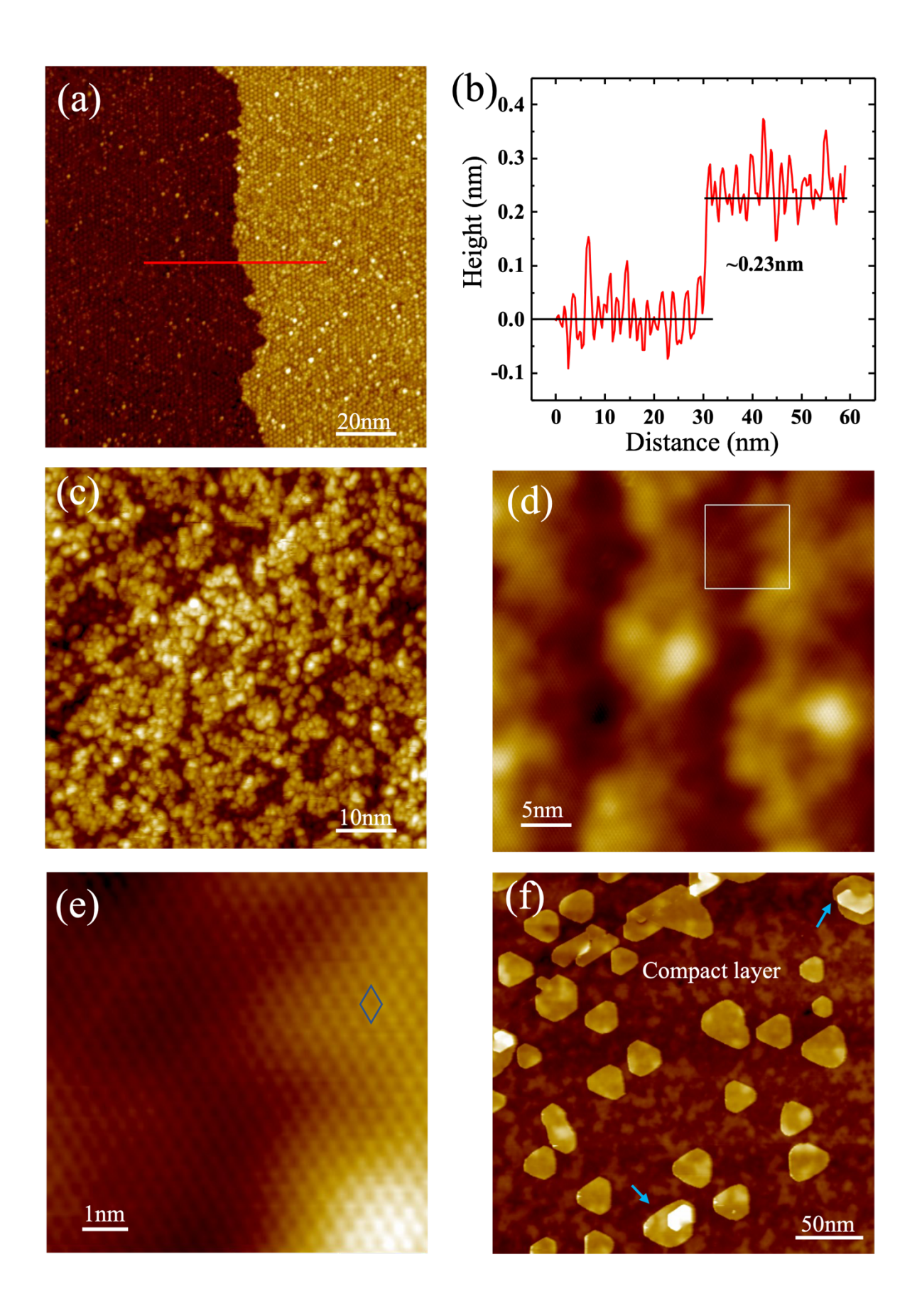


Figure 1. Characterization of growth morphology of SnSe₂ on STO(111). (a) Large scale STM image ($V_s = 2 \text{ V}$, $I_t = 5 \text{ pA}$) where the majority of the STO(111) surface forms 3×3 surface reconstruction. (b) Line profile across the red trace in (a), revealing the single step height of the STO(111) surface. (c) STM image ($V_s = 2.5 \text{ V}$, $I_t = 5 \text{ pA}$) showing the granular (e.g., cluster-like) growth of the SnSe₂ wetting layer that passivates the STO surface. (d) STM image ($V_s = 0.6 \text{ V}$, $I_t = 150 \text{ pA}$) illustrating the formation of continuous SnSe₂ compact layer beyond the wetting layer, which conforms to the substrate features such as steps of the STO(111) substrate. (e) Zoom-in STM image ($V_s = 0.6 \text{ V}$, $I_t = 150 \text{ pA}$) of the white box in (d), illustrating the lattice continuity across a substrate step with SnSe₂ unit cell labelled by blue rhombic. The film exhibits relatively low density of atomic defects. (f) STM image ($V_s = 2 \text{ V}$, $I_t = 5 \text{ pA}$) displaying the formation of second layer islands on top of the compact SnSe₂ film. Blue arrows point to the islands that are evolving into spirals.

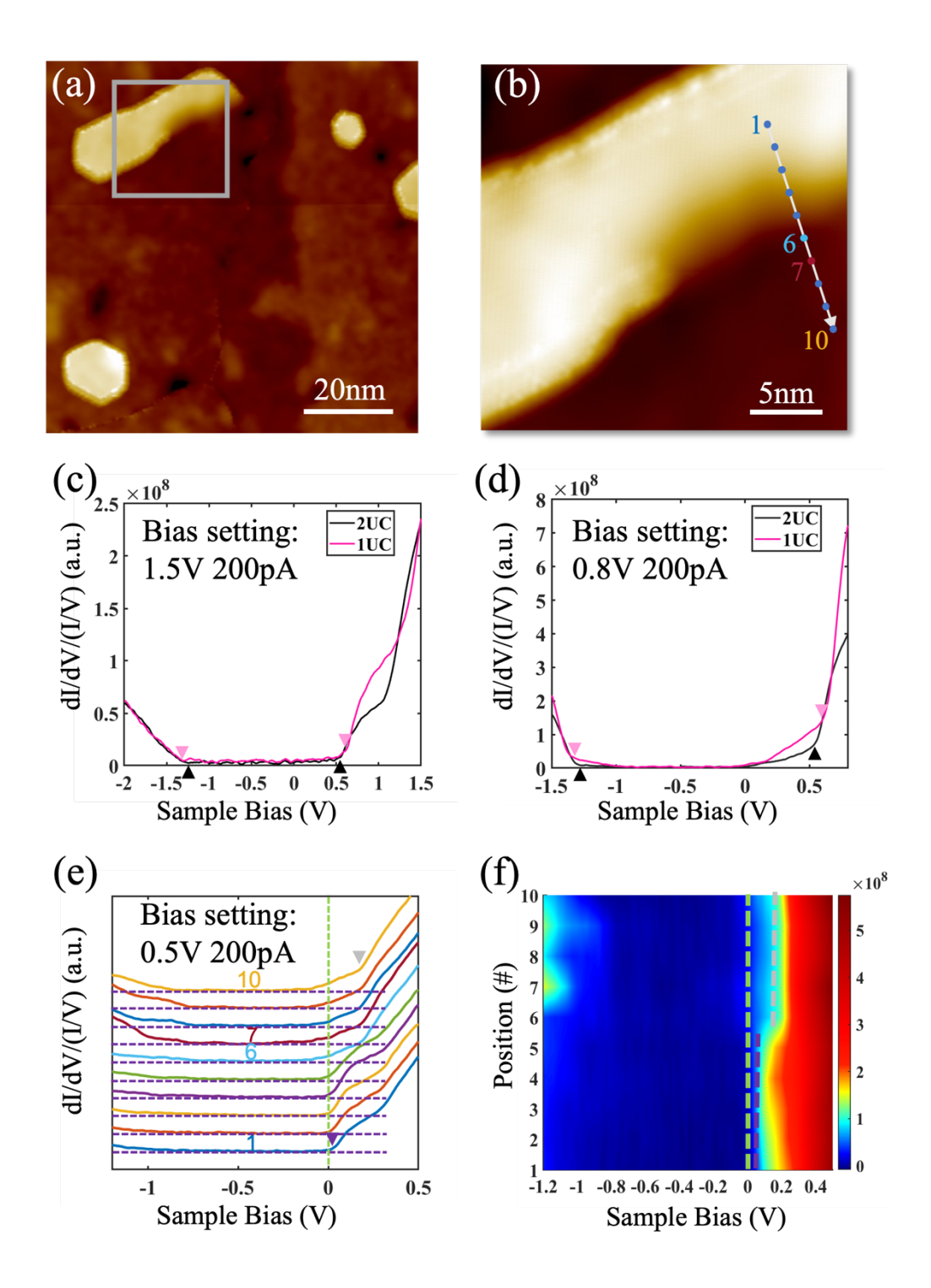


Figure 2. Charge transfer and electronic structure evolution across a "spiral"-grown SnSe₂ island. (a) Large scale STM image $(V_s = 2.5 \text{ V}, I_t = 5 \text{ pA})$ showing the coexistence of second layer SnSe₂ islands that are either stand-alone or partially connected to the first layer. Zoom-in image of the grey box is shown in (b) $(V_s = 0.8 \text{ V}, I_t = 100 \text{ pA})$. (c-d) Normalized STS spectra taken on the monolayer (1UC, pink) and bilayer (2UC, black) SnSe₂ films at relatively large tip-sample distances. The pink and black triangles mark CBM' and VBM originating at the Γ point of the momentum space of 1UC and 2UC, respectively. (e) Normalized STS spectra taken along the white line in (b) from the second layer to the first layer at a reduced tip-sample distance, where CBM at the M point (larger parallel momentum) is identified, along with the emergence of a DOS tail penetrating through the Fermi level. The horizontal dashed lines provide eye guide for the ground of each spectrum. The grey and purple triangles mark the CBM position of the 1st and 2nd layer, respectively. (f) Corresponding DOS heatmap from STS spectra in (e) with x-axis, y-axis, and color contrast representing sample bias, point number, and intensity of DOS, respectively. Green dashed lines mark the Fermi level position in (e-f), and the grey and purple dashed lines in (f) mark the CBM position of the 1st and 2nd layer, respectively.

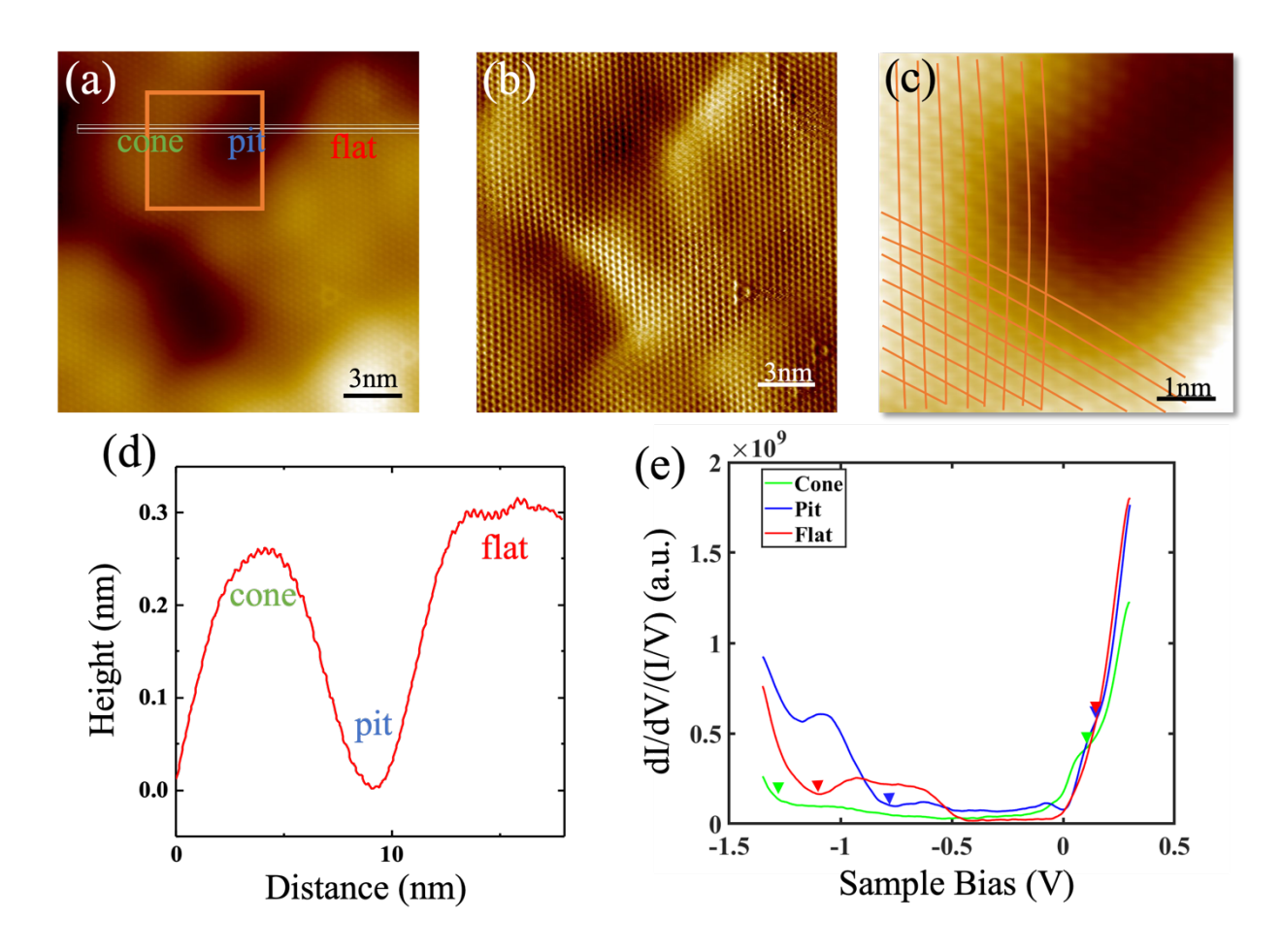


Figure 3. Strain variation in the as grown SnSe₂ film. (a) STM image ($V_s = 0.8 \text{ V}$, $I_t = 100 \text{ pA}$) of the SnSe₂ compact layer on top of a STO terrace, which reveals a pronounced height variation. The lattice continuity is clearly resolved in the current image ($V_s = 0.6 \text{ V}$, $I_t = 150 \text{ pA}$) in (b). (c) The local lattice distortions in the SnSe₂ film are illustrated in the zoom-in image (from the brown box in (a)), with the lines drawn to track the atom positions. (d) The height profile along the white trace in (a), where the cone, pit and flat regions are marked accordingly. (e) STS spectra (setpoint: $V_s = 0.3 \text{ V}$, $I_t = 200 \text{ pA}$) taken at the cone, pit, and flat regions, respectively. The arrows mark the onsets of CBM(M) and VBM(Γ).

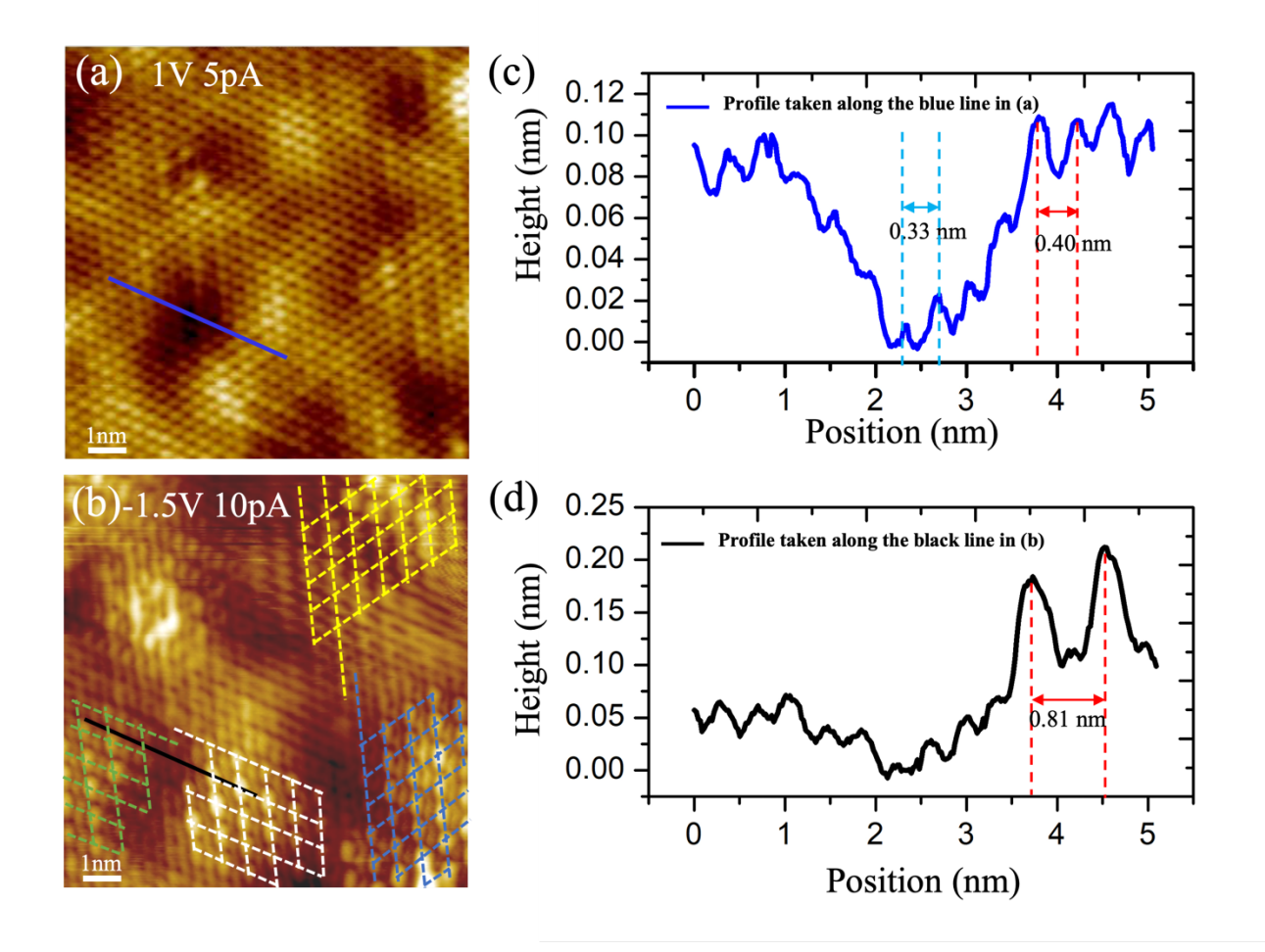


Figure 4. Charge density wave variations in the SnSe₂ compact layer on STO. (a) STM image $(V_s = 1.0 \text{ V}, I_t = 5 \text{ pA})$ of the SnSe₂ compact layer. (b) At a different bias $(V_s = -1.5 \text{ V}, I_t = 10 \text{ pA})$, the locally commensurate 2×2 CDW domains are observed, as outlined by the dotted meshes following the high symmetry directions of SnSe₂, that are separated by phase slips. The tip is functionalized to reveal the details of the CDW patterns. (c-d) Line-profile measurements across the blue and black marks in (a,b). Note that the two marks are at the same location. Dashed lines in (c) indicate the lattice constants in the pit and the cone areas, which are compressive and tensile strained, respectively. The 2×2 CDW periodicity on the cone area is indicated in (d).

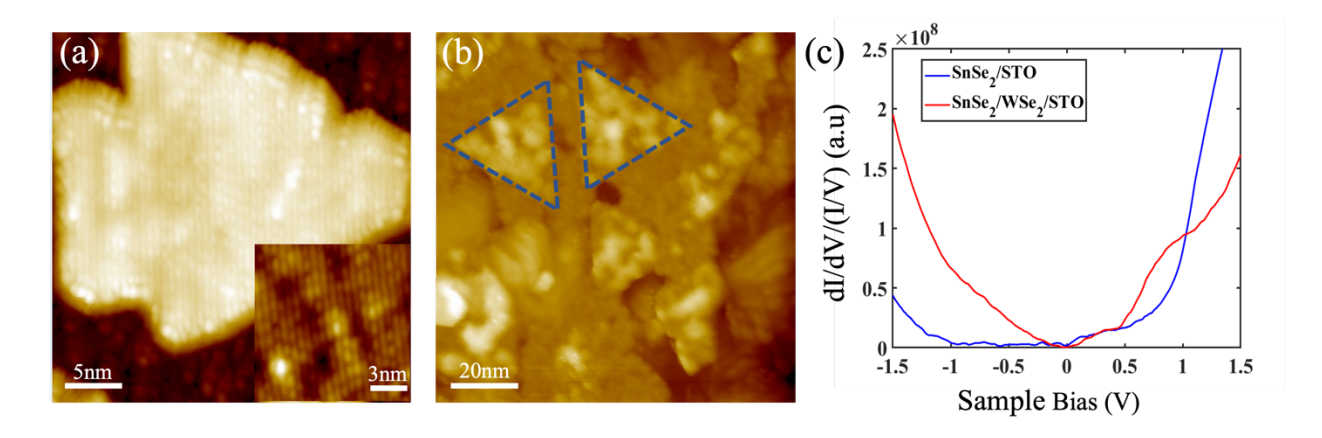
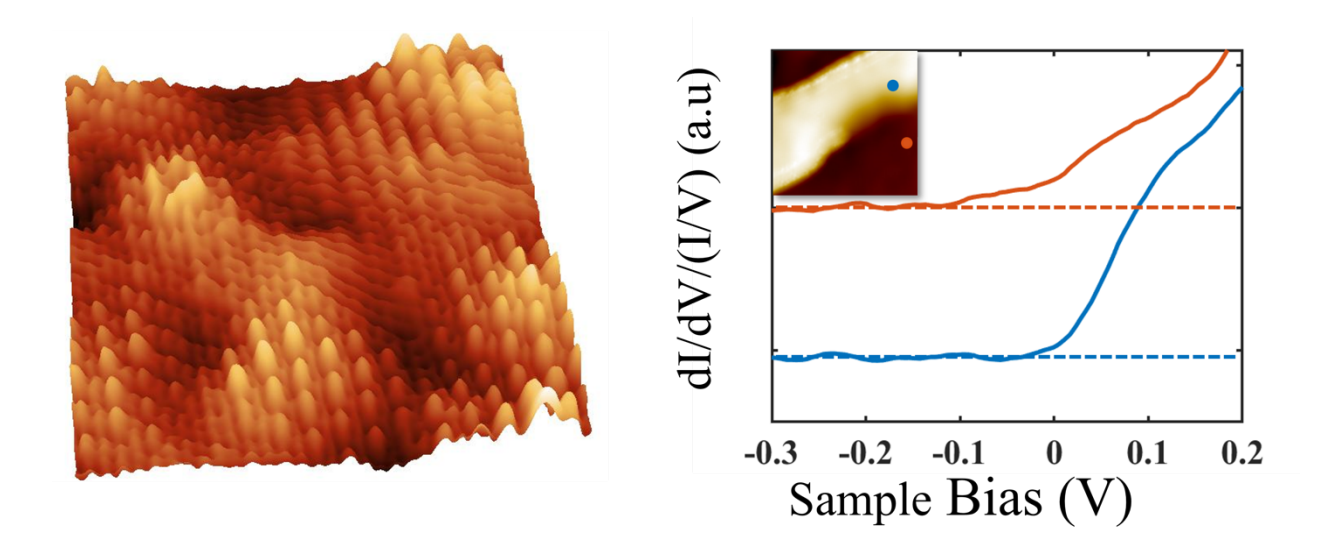


Figure 5. Electronic structures of SnSe₂/STO vs. SnSe₂/1T'-WSe₂/STO. (a) STM images ($V_s = 1 \text{ V}$, $I_t = 20 \text{ pA}$) of 1T'-WSe₂/STO showing characteristic stripe-like feature. Inset is the zoom-in image of the stripe structure. (b) STM image ($V_s = 2 \text{ V}$, $I_t = 5 \text{ pA}$) taken after the growth of a monolayer SnSe₂ on the STO with partially covered 1T'-WSe₂. The dashed blue triangles in (b) highlight the 1T'-WSe₂ islands underneath the monolayer SnSe₂. (c) STS spectra (setpoint: $V_s = 1.3 \text{ V}$, $I_t = 150 \text{ pA}$) taken on the SnSe₂/STO and SnSe₂/1T'-WSe₂/STO regions with the latter behaving more metallic.



TOC Graphic